

¹ **Relative effect of host versus non-host vegetation structure on for-**
² **est insect severity depends on climatic water deficit**

³ Michael J. Koontz^{1,2,*}, Andrew M. Latimer^{1,2}, Leif A. Mortenson³, Christopher J. Fettig³, Constance I.
⁴ Millar⁴, Malcolm P. North^{1,2,5}

⁵ ¹Graduate Group in Ecology, University of California, Davis, CA, USA

⁶ ²Department of Plant Sciences, University of California, Davis, CA, USA

⁷ ³USDA Forest Service, Pacific Southwest Research Station, Placerville, CA, USA

⁸ ⁴USDA Forest Service, Pacific Southwest Research Station, Albany, CA, USA

⁹ ⁵USDA Forest Service, Pacific Southwest Research Station, Davis, CA, USA

¹⁰ *Correspondence: michael.koontz@colorado.edu

¹¹ Date report generated: March 31, 2019

¹² **Abstract**

¹³ Forest insects are a primary mortality agent of trees in Sierra Nevada mixed-conifer forests. The recent hot
¹⁴ drought from 2012 to 2015 led to massive tree die-off throughout the state of California, and especially in the
¹⁵ Sierra Nevada.

¹⁶ **Introduction**

¹⁷ Aggressive bark beetles dealt the final blow to many of the nearly 150 million trees killed in the California
¹⁸ drought of 2012 to 2015 and its aftermath (USDAFS 2019). A harbinger of climate change effects to come,
¹⁹ high temperatures exacerbating the extreme drought led to tree mortality events of unprecedented size in the
²⁰ driest, densest forests across the state (Millar and Stephenson 2015, Young et al. 2017). A century of fire
²¹ suppression policy has enabled forests to grow unchecked into dense stands, which increases water stress on
²² trees and makes them more vulnerable to bark beetle attack (Fettig 2012, North et al. 2015).

²³ Previous studies show that bark beetles thrive in denser forests (Fettig 2012), but density is often a coarse
²⁴ gauge of the size and spatial distribution of trees— the forest structure— with which bark beetles interact
²⁵ (Raffa et al. 2008).

²⁶ Recent research has shown a strong link between complex forest structure and forest resilience, but measuring
²⁷ this complexity generally requires expensive equipment or labor-intensive field surveys (Larson and Churchill
²⁸ 2012, Kane et al. 2014). These barriers restrict survey frequency and extent, which limits insights into

29 phenomena like bark beetle outbreaks that rapidly emerge over weeks to months but have long-lasting effects
30 on forest conditions.

31 Further, the clear and vast latitudinal gradient of mortality challenges our ability to simultaneously consider
32 how environmental conditions may interact with local forest structure to produce patterns of insect activity.

33 along a strong south to north latitudinal gradient (Young et al. 2017, USDAFS 2019).

34 Latitudinal and elevational gradients in the intensity of bark beetle activity during the recent California
35 drought provide unique opportunities for a postmortem analysis of a major tree die off and how intersecting
36 forces of forest structure and environmental conditions affect disturbance dynamics. Quantitative, fine-scale
37 measures of tree condition across these geographic gradients will enable broad-scale assessment of forest
38 structure as well as the intensity of western pine beetle-induced tree mortality. Combined, these measurements
39 can better our understanding of how complex forest structure affects insect disturbance, and vice versa, across
40 the Sierra Nevada. Sound forest management requires a better understanding of the relationships between
41 forest spatial structure, environmental conditions, and disturbance, which ultimately depends on accurate
42 measurement of forest structure at appropriate spatial scales.

43 **How forest structure affects bark beetle activity**

44 Water stress and competition (Hayes et al. 2009, Young et al. 2017) Host availability (ease of dispersal to
45 new hosts) Beetles prefer larger trees under outbreak conditions

46 Forests in California's Sierra Nevada region are characterized by regular bark beetle disturbances that interact
47 with forest structure. Bark beetles shape forest structure as they sporadically kill weakened trees under
48 normal conditions, or wide swaths of even healthy trees under outbreak conditions. Forest structure also
49 strongly influences bark beetle activity. Low-density forests are less prone to bark beetle attacks, but resolving
50 the mechanism underlying this observation requires a more nuanced view of forest structure. For instance, a
51 low-density forest may resist attack because its trees are in smaller clumps with greater average tree vigor,
52 or because its wider canopy openings disrupt pheromone signaling between beetles (Fettig 2012). Thus, it
53 remains poorly understood how complex forest structure affects and is affected by bark beetle activity.

54 Forest spatial structure, the size and distribution of trees in the forest, is thought to be a key determinant of
55 forest resilience. To date, much of the work on Sierra Nevada forest resilience focuses on stem density, which
56 belies the complexity of forest structure and how it interacts with disturbance. However, complex forest
57 structure is challenging to quantify, as it requires labor-intensive field surveys (e.g., to generate stem maps)
58 or highly specialized, expensive equipment (e.g., LiDAR). Small, unmanned aerial systems (sUAS) enable

59 fast and relatively cheap remote imaging over dozens of hectares of forest, which can be used to determine
60 both forest structure and tree condition at the individual tree scale. Implementing photogrammetry on the
61 collected images can provide a rich picture of the complex, 3-dimensional forest structure to which bark
62 beetles respond, and equipping the sUAS with a multispectral sensor will allow calculation of vegetation
63 indices (e.g., NDVI) commonly used to assess tree condition.

64 Use drones for insect attack studies! (Morris et al. 2017).

65 Climate change mitigation strategies emphasize reducing tree densities (North et al. 2015, Young et al. 2017),
66 but understanding the optimal scale and pattern of tree distribution that can mitigate bark beetle outbreaks
67 will be vital for predicting how California forests may respond to these interventions. This project investigates
68 this relationship with the following research questions:

- 69 1. How does local host tree density and size affect the severity of western pine beetle disturbance?
- 70 2. How does total tree density and size affect the severity of western pine beetle disturbance?
- 71 3. How does environmentally-driven tree moisture stress affect the severity of western pine beetle distur-
72 bance?
- 73 4. Do the effects of forest structure and environmental condition on western pine beetle disturbance
74 interact?

75 We used ultra-high resolution remote sensing data from a small, unhumanned aerial system (sUAS, aka
76 drone) over a network of 32 sites in the Sierra Nevada spanning 1000m of elevation and 350km of latitude and
77 covering a total of 9 square kilometers of forest to ask how fine-scale forest structure affected the probability
78 of tree mortality during the cumulative mortality event of 2012 to 2018.

79 Methods

80 Study system

81 The study sites comprise mostly ponderosa pine trees, *Pinus ponderosa*, whose primary bark beetle predator
82 in California is the western pine beetle (WPB), *Dendroctonus brevicomis*. The WPB is an aggressive bark
83 beetle, meaning it must attack and kill live trees in order to successfully reproduce (Raffa et al. 2008).
84 Pioneer WPBs disperse to a new host tree, determine the host's susceptibility to attack, and use pheromone
85 signals to attract other WPBs. The attracted WPBs mass attack the tree by boring into its inner bark,
86 laying eggs, and dying, leaving their offspring to develop inside the doomed tree before themselves dispersing
87 (Raffa et al. 2008). Small WPB populations prefer weakened trees but large populations can overwhelm

88 the defense mechanisms of even healthy trees. Successful attacks on large, healthy trees are boons to bark
89 beetle fecundity and trigger outbreaks in which populations explode and massive tree mortality occurs. In
90 California, the WPB can have 3 generations in a single year giving it a greater potential to spread rapidly
91 through forests than its more infamous congener, the mountain pine beetle, *Dendroctonus ponderosa* (MPB).

92 We built our study on 180 vegetation monitoring plots at 36 sites established between 2016 and 2017 (Fettig
93 et al. 2019). These established plots are located in beetle-attacked, mixed-conifer forests across the Eldorado,
94 Stanislaus, Sierra and Sequoia National Forests across an elevation gradient (3000-4000 feet, 4000-5000 feet,
95 and 5000+ feet above sea level) and have variable forest structure and disturbance history. Plot locations
96 were selected specifically in areas with >40% ponderosa pine basal area and >10% ponderosa pine mortality.
97 The 0.04ha circular plots are clustered along transects in groups of 5, with between 80 and 200m between
98 each plot. All trees within the plot were assessed as dead or alive. The stem location of all trees was mapped
99 relative to the center of each plot using azimuth/distance measurements. Tree identity to species and diameter
100 at breast height (dbh) were recorded if dbh was greater than 6.35cm. During the spring and early summer of
101 2018, all field plots were revisited to assess whether dead trees had fallen.

102 **Instrumentation**

103 Imagery was captured using a DJI Zenmuse X3 RGB camera (DJI 2015a) and a Micasense RedEdge3 5-band
104 multispectral camera (Micasense 2015). We mounted both of these instruments simultaneously on a DJI
105 Matrice 100 aircraft (DJI 2015b) using the DJI 3-axis stabilized gimbal for the Zenmuse X3 camera and a
106 Micasense angled fixed mount for the RedEdge3 camera. The gimbal and the angled fixed mount ensured
107 both instruments were nadir-facing during image capture. Just prior or after image capture at each site, we
108 calibrated the RedEdge3 camera by taking an image of a calibration panel on the ground in full sun with
109 known reflectance values for each of the 5 narrow bands.

Table 1: Reflectance sensitivity of the Micasense Rededge3 camera. The calibration panel value represents the reflectance of the calibration panel for the given wavelength.

Band number	Band name	Center wavelength	Band width	Wavelength range	Panel reflectance
1	blue (b)	475	20	465-485	0.64
2	green (g)	560	20	550-570	0.64
3	red (r)	668	10	663-673	0.64
4	near infrared (nir)	840	40	820-860	0.60

Band number	Band name	Center wavelength	Band width	Wavelength range	Panel reflectance
5	red edge (re)	717	10	712-722	0.63

110 **Flight protocol**

111 Image capture was conducted as close to solar noon as possible to minimize shadow effects (always within 4
 112 hours; usually within 2 hours). Prior to the aerial survey, two strips of bright orange drop cloth (~100cm x
 113 15cm) were positioned as an “X” over the permanent monuments marking the center of the 5 field plots from
 114 Fettig et al. (2019).

115 For each of the 36 sites (containing 5 plots each), we captured imagery over the surrounding ~40 hectares of
 116 forested area using north-south aerial transects. For XXXXX sites, we surveyed less surrounding area in
 117 order to maintain visual and radio communication with the aircraft during flight (Table XXXXXX).

118 Table XXXX. Columns: Site, forest, elevation, rep, surveyed area, survey date

119 We preprogrammed transect paths using Map Pilot for DJI on iOS (hereafter Map Pilot) (Easy 2018). All
 120 transects tracked the terrain and their altitude remained approximately constant at 120 meters above ground
 121 level in order to maintain consistent ground sampling distance in the imagery. Ground level was based on a
 122 1-arc-second digital elevation model (Farr et al. 2007) and we implemented terrain following using Map Pilot.
 123 For this analysis, we dropped 4 sites whose imagery was of insufficient quality to process.

124 Structure from motion (SfM) processing requires highly overlapping images, especially in densely vegetated
 125 areas. We planned transects with 90% forward overlap and 90% side overlap at 100 meters below the lens.
 126 Thus, with flights being at 120 meters above ground level, we achieved slightly higher than 90/90 overlap for
 127 objects 20 meters tall or shorter. Overlap values were based on focal length and field of view parameters
 128 of the Zenmuse X3 camera. Images were captured at a constant rate of 1 image every 2 seconds for both
 129 cameras. A forward overlap of 90% at 100 meters translates to a flight speed of approximately 6.3 m/s and a
 130 side overlap of 90% at 100 meters translates to transects approximately 18 meters apart. Approximately
 131 1900 photos were captured over each 40 hectare survey area for each camera.

132 **Structure from motion/Photogrammetric processing**

133 We used structure from motion (SfM), aka photogrammetry, to generate orthorectified reflectance maps,
 134 digital surface models, and dense point clouds for each field site. We used Pix4Dmapper Cloud to process
 135 imagery using parameters ideal for images of a densely vegetated area taken by a multispectral camera.

136 For three sites, we processed the RGB and the multispectral imagery in the same project to enhance the
137 resolution of the dense point cloud. All SfM projects resulted in a single processing “block,” indicating that
138 all images in the project were optimized and processed together.

139 **Creating canopy height models**

140 We classified each survey area’s dense point cloud into “ground” and “non-ground” points using a cloth
141 simulation filter algorithm (Zhang et al. 2016) implemented in the **lidR** (Roussel et al. 2019) package. We
142 rasterized the ground points using the **raster** package (Hijmans et al. 2019) to create a digital terrain model
143 representing the ground underneath the vegetation at 1 meter resolution. We created a canopy height model
144 by subtracting the digital terrain model from the digital surface model created in Pix4Dmapper.

145 **Tree detection**

146 We tested a total of 7 automatic tree detection algorithms and a total of 177 parameter sets on the canopy
147 height model or the dense point cloud to locate trees within each site (Table XXXXX; algorithm, number of
148 parameter sets, reference). We used 3 parameter sets of a variable window filter implmented in **ForestTools**
149 (Plowright 2018) including the default variable window filter function in **ForestTools** as well as the “pines”
150 and “combined” functions from Popescu and Wynne (2004). We used 6 parameter sets of a local maximum
151 filter implemented in **lidR**. We used 131 parameter sets of the algorithm from Li et al. (2012), which operates
152 on the original point cloud. These parameter sets included those from Shin et al. (2018) and Jakubowski et
153 al. (2013). We used 3 parameter sets of the **watershed** algorithm implemented in **lidR**, which is a wrapper
154 for a function in the **EBImage** package (Pau et al. 2010). We used 3 parameter sets of **ptrees** (Vega et al.
155 2014) implemented in **lidR** (Roussel et al. 2019) and **lidRplugins** (Roussel 2019) and which operates on
156 the raw point cloud, without first normalizing it to height above ground level (i.e.. subtracting the ground
157 elevation from the dense point cloud). We used the default parameter set of the **multichm** (Eysn et al. 2015)
158 algorithm implmented in **lidR** (Roussel et al. 2019) and **lidRplugins** (Roussel 2019). We used 30 parameter
159 sets of the experimental algorithm **lmfx** (Roussel 2019).

160 **Map ground data**

161 Each orthorectified reflectance map was inspected to locate the 5 orange “X”s marking the center of the
162 field plots. We were able to locate 110 out of 180 field plots and were then able to use these plots for
163 validation of automated tree detection algorithms. We used the **sf** package (Pebesma et al. 2019) to convert
164 distance-from-center and azimuth measurements of each tree in the ground plots to an x-y position on the
165 SfM-derived reflectance map using the x-y position of the orange X visible in the reflectance map as the

166 center.

167 **Correspondence of automatic tree detection with ground data**

168 We calculated 7 forest structure metrics for each field plot using the ground data collected by Fettig et al.
169 (2019): total number of trees, number of trees greater than 15 meters, number of trees less than 15 meters,
170 mean height of trees, 25th percentile tree height, 75th percentile tree height, mean distance to nearest tree
171 neighbor, mean distance to 2nd nearest neighbor.

172 For each tree detection algorithm and parameter set described above, we calculated the same set of 7 structure
173 metrics within the footprint of the validation field plots. We calculated the Pearson's correlation and root
174 mean square error (RMSE) between the ground data and the aerial data for each of the 7 structure metrics
175 for each of the 177 automatic tree detection algorithms/parameter sets.

176 For each algorithm and parameter set, we calculated its performance relative to other algorithms as whether
177 its Pearson's correlation was within 5% of the highest Pearson's correlation as well as whether its RMSE was
178 within 5% of the lowest RMSE. For each algorithm/parameter set, we summed the number of forest structure
179 metrics for which it reached these 5% thresholds. For automatically detecting trees across the whole study,
180 we selected the algorithm/parameter set that performed well across the most number of forest metrics.

181 **Segmentation of crowns**

182 We delineated individual tree crowns with a marker controlled watershed segmentation algorithm (Meyer and
183 Beucher 1990) using the detected treetops as markers implemented in the `ForestTools` package (Plowright
184 2018). If the automatic segmentation algorithm failed to generate a crown segment for a detected tree (e.g.,
185 often snags with a very small crown footprint), a circular crown was generated with a radius of 0.5 meters. If
186 the segmentation generated multiple polygons for a single detected tree, only the polygon containing the
187 detected tree was retained. Image overlap decreases near the edges of the overall flight path, which reduces
188 the quality of the SfM processing in those areas. Thus, we excluded segmented crowns within 35 meters of
189 the edge of the survey area.

190 We used the `velox` package (Hunziker 2017) to extract all the pixel values from the orthorectified reflectance
191 map for each of the 5 narrow bands within each segmented crown polygon. Per pixel, we additionally
192 calculated the normalized difference vegetation index (NDVI; Rouse et al. (1973)), the normalized difference
193 red edge (NDRE; Gitelson and Merzlyak (1994)), the red-green index (RGI; Coops et al. (2006)), the red
194 edge chlorophyll index (CI[red edge]; Clevers and Gitelson (2013)), and the green chlorophyll index (CI[green];
195 Clevers and Gitelson (2013)). For each crown polygon, we calculated the mean value for each raw and derived

196 reflectance band (5 raw; 5 derived).

197 **Classification of trees**

198 We overlaid the segmented crowns on the reflectance maps from 20 sites spanning the latitudinal and
199 elevational gradient in the study. Using QGIS, we hand classified XXXX trees as live/dead and as one
200 of 5 dominant species in the study area (*Pinus ponderosa*, *Pinus lambertiana*, *Abies concolor*, *Calocedrus*
201 *decurrens*, or *Quercus kelloggii*) using the mapped ground data as a guide.

202 We used all 10 mean values of the reflectance bands for each tree crown polygon to predict whether the hand
203 classified trees were alive or dead using a boosted logistic regression model implemented in the **caret** package
204 (Kuhn 2008). For just the living trees, we similarly used all 10 reflectance values to predict the tree species
205 using regularized discriminant analysis implemented in the **caret** package, which proved to have the highest
206 accuracy for a training dataset (accuracy = XXXXX, kappa = XXXXX).

207 Finally, we used these models to classify all tree crowns in the data set as alive or dead as well as the species
208 of living trees.

209 **Allometric scaling of height to basal area**

210 We converted the height of each tree determined using the canopy height model to its basal area. Using
211 the tree height and diameter at breast height (DBH; breast height = 1.37m) ground data from Fettig et al.
212 (2019), we fit a simple linear regression to predict DBH from height for each of the 5 dominant species. Using
213 the model-classified tree species of each segmented tree, we used the corresponding linear relationship for
214 that species to estimate the DBH given the tree's height. We then calculated each tree's basal area, assuming
215 no tapering from breast height.

216 **Note on assumptions about dead trees**

217 For the purposes of this study, we assumed that all dead trees were ponderosa pine and were thus host trees.
218 This is a reasonably good assumption, given that Fettig et al. (2019) found that 73.4% of the dead trees in
219 the coincident ground plots were ponderosa pine.

220 **Rasterizing individual tree data**

221 Because the tree detection algorithms were validated against ground data at the plot level, we rasterized the
222 classified trees at a spatial resolution similar to that of the ground plots (rasterized to 20m x 20m equalling
223 400 m²; circular ground plots with 11.35m radius equalling 404 m²). In each raster cell, we tallied: number

224 of alive trees, number of dead trees, number of ponderosa pine trees, number of non-ponderosa pine trees,
225 basal area of ponderosa pine trees, basal area of non-ponderosa pine trees.

226 **Environmental data**

227 We used climatic water deficit (CWD) (Stephenson 1998) from the 1980-2010 mean value of the basin
228 characterization model (Flint et al. 2013) as an integrated measure of temperature and moisture conditions
229 for each cell. Higher values of CWD correspond to hotter, drier conditions and lower values correspond
230 to cooler, wetter conditions CWD has been shown to correlate well with broad patterns of tree mortality
231 in the Sierra Nevada (Young et al. 2017). We resampled the climatic water deficit product using bilinear
232 interpolation implemented in the `raster` package to match the 20m x 20m spatial scale of the other variables.
233 We converted the CWD value for each cell into a z-score representing that cell's deviation from the mean
234 CWD across the climatic range of Sierra Nevada ponderosa pine as determined from XXXXX herbarium
235 records described in Baldwin et al. (2017). Thus, a CWD z-score of one would indicate that the CWD at
236 that cell is one standard deviation hotter/drier than the mean CWD across all geolocated herbarium records
237 for ponderosa pine in the Sierra Nevada.

238 **Statistical model**

239 We used a generalized linear model with a zero-inflated binomial response and a logit link to predict the
240 probability of ponderosa pine mortality within each raster cell as a function of the crossed effects of ponderosa
241 pine quadratic mean diameter and density added to the crossed effect of overall quadratic mean diameter and
242 density as well as the interaction of each summand with climatic water deficit at each site.

243 To measure and account for spatial autocorrelation of the bark beetle behavioral processes underlying
244 ponderosa mortality, we first subsampled the data at each site to a random selection of 200, 20m x 20m
245 cells representing approximately 27.5% of the surveyed area. With these subsampled data, we included a
246 separate exact Gaussian process term per site of the interaction between the x- and y-position of each cell
247 using the `gp()` function in the `brms` package (Bürkner 2017). The Gaussian process accounts for spatial
248 autocorrelation in the model by jointly estimating the spatial covariance of the response variable with the
249 effects of the other covariates.

$$y_{i,j} \sim \begin{cases} 0, & p \\ Binom(n_i, \pi_i), & 1 - p \end{cases}$$

logit(π_i) = $\beta_0 +$

$\beta_1 X_{cwd,j} +$

$\beta_1 X_{cwd,j} (\beta_2 X_{pipoQMD,i} + \beta_3 X_{pipoDensity,i} + \beta_4 X_{pipoQMD,i} X_{pipoDensity,i}) +$

$\beta_1 X_{cwd,j} (\beta_5 X_{overallQMD,i} + \beta_6 X_{overallDensity,i} + \beta_7 X_{overallQMD,i} X_{overallDensity,i}) +$

$\mathcal{GP}_j(x_i, y_i)$

250 Where y_i is the number of dead trees in cell i , n_i is the sum of the dead trees and live ponderosa pine trees
 251 in cell i , π_i is the probability of ponderosa pine tree mortality in cell i , p is the probability of there being
 252 zero dead trees in a cell arising as a result of an unmodeled process, $X_{cwd,j}$ is the z-score of climatic water
 253 deficit for site j , $X_{pipoQMD,i}$ is the scaled quadratic mean diameter of ponderosa pine in cell i , $X_{pipoDensity,i}$
 254 is the scaled density of ponderosa pine trees in cell i , $X_{overallQMD,i}$ is the scaled quadratic mean diameter
 255 of all trees in cell i , $X_{overallDensity,i}$ is the scaled density of all trees in cell i , x_i and y_i are the x- and y-
 256 coordinates of the centroid of the cell in an EPSG3310 coordinate reference system, and \mathcal{GP}_j represents the
 257 exact Gaussian process describing the spatial covariance between cells at site j .

258 We used 4 chains with 2000 iterations each (1000 warmup, 1000 samples), and confirmed chain convergence
 259 by ensuring all `Rhat` values were less than 1.1 (Brooks and Gelman 1998). We used posterior predictive
 260 checks to visually confirm model performance by overlaying the density curves of the predicted number of
 261 dead trees per cell over the observed number (Gabry et al. 2019). We used 50 random samples from the
 262 model fit to generate 50 density curves and ensured curves were centered on the observed distribution, paying
 263 special attention to model performance at capturing counts of zero.

264 Software and data availability

265 All data are available via the Open Science Framework. Statistical analyses were performed using the `brms`
 266 packages. With the exception of the SfM software (Pix4Dmapper Cloud) and the GIS software QGIS, all
 267 data carpentry and analyses were performed using R (R Core Team 2018).

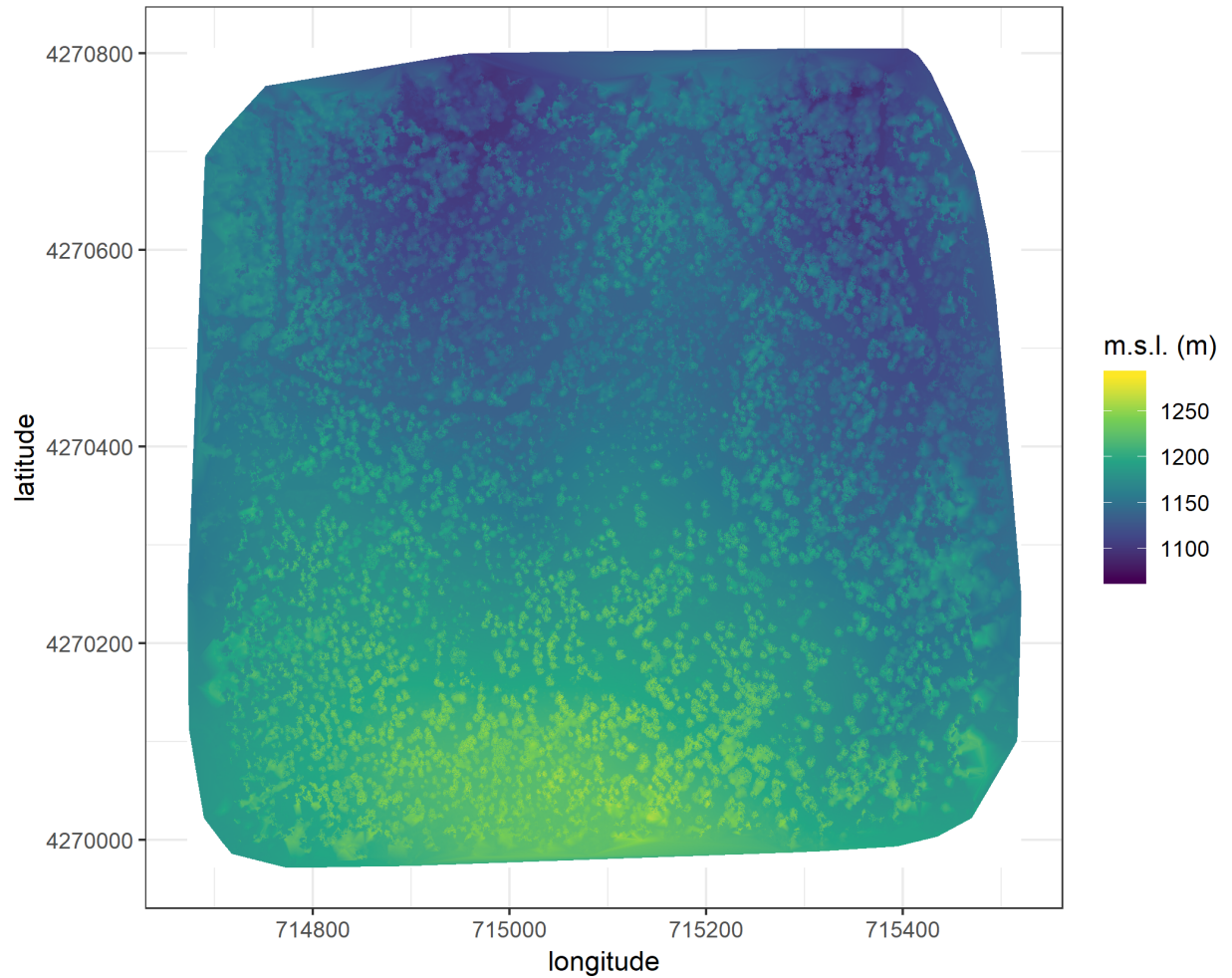


Figure 1: Example digital surface model (DSM) that is a direct output from the dense point cloud generated using structure from motion (SfM) processing. The DSM represents the ground elevation plus the vegetation height.

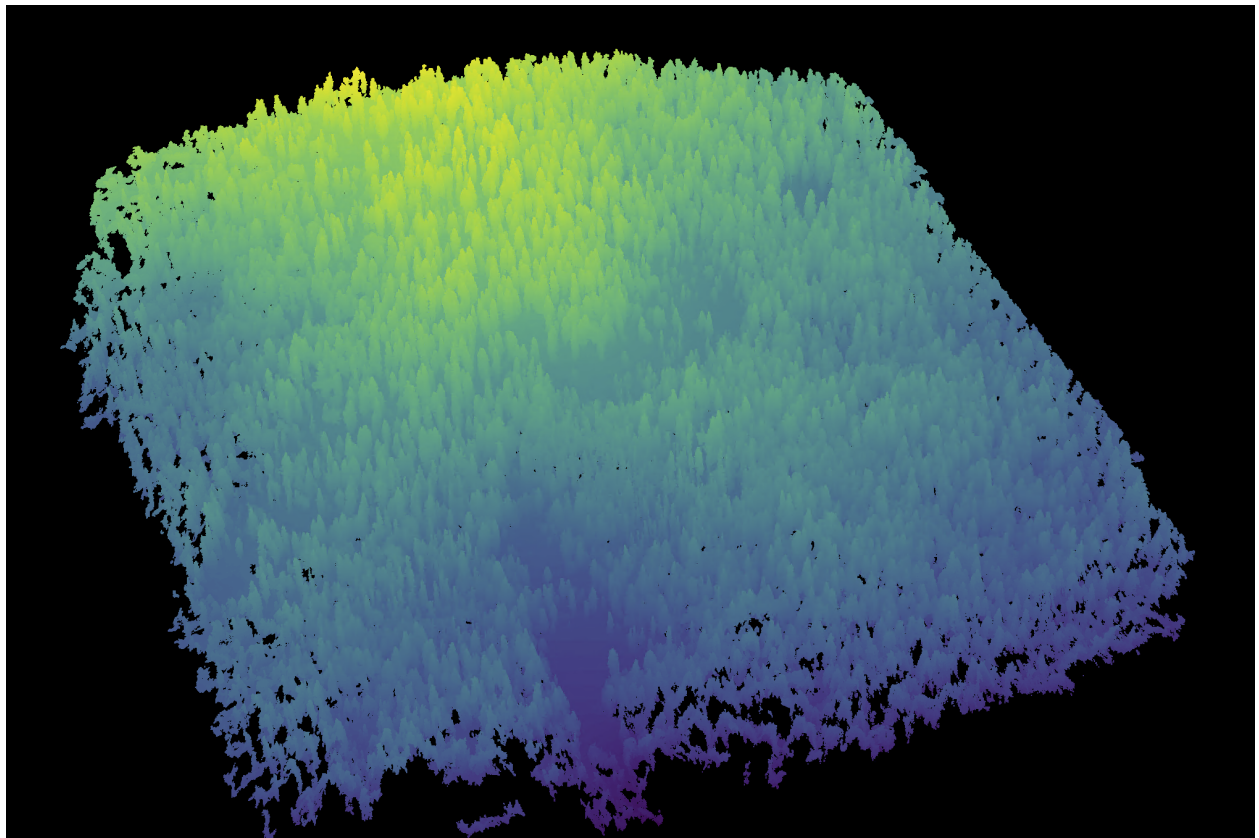


Figure 2: Point cloud from Pix4D

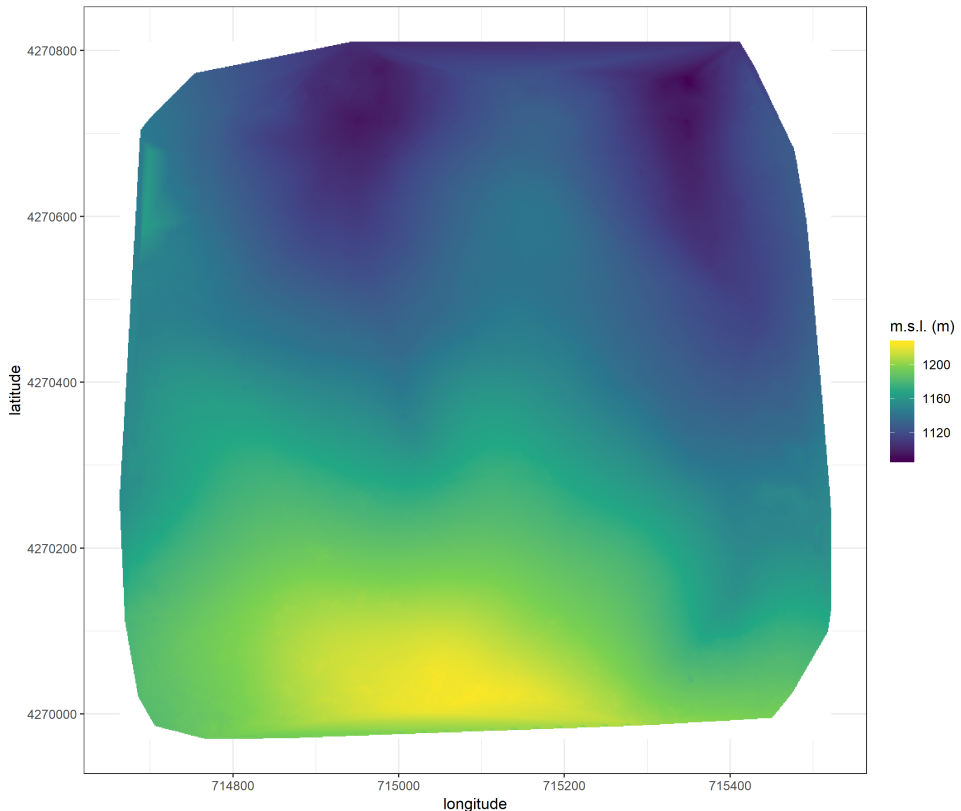


Figure 3: Example digital terrain model (DTM) resulting from processing the digital surface model using the cloth simulation filter algorithm (Zhang et al. 2016), which classifies points in the dense point cloud as “ground” or “not-ground” and then interpolates the “ground” elevation for the rest of the dense point cloud footprint. The DTM represents the ground elevation without any vegetation.

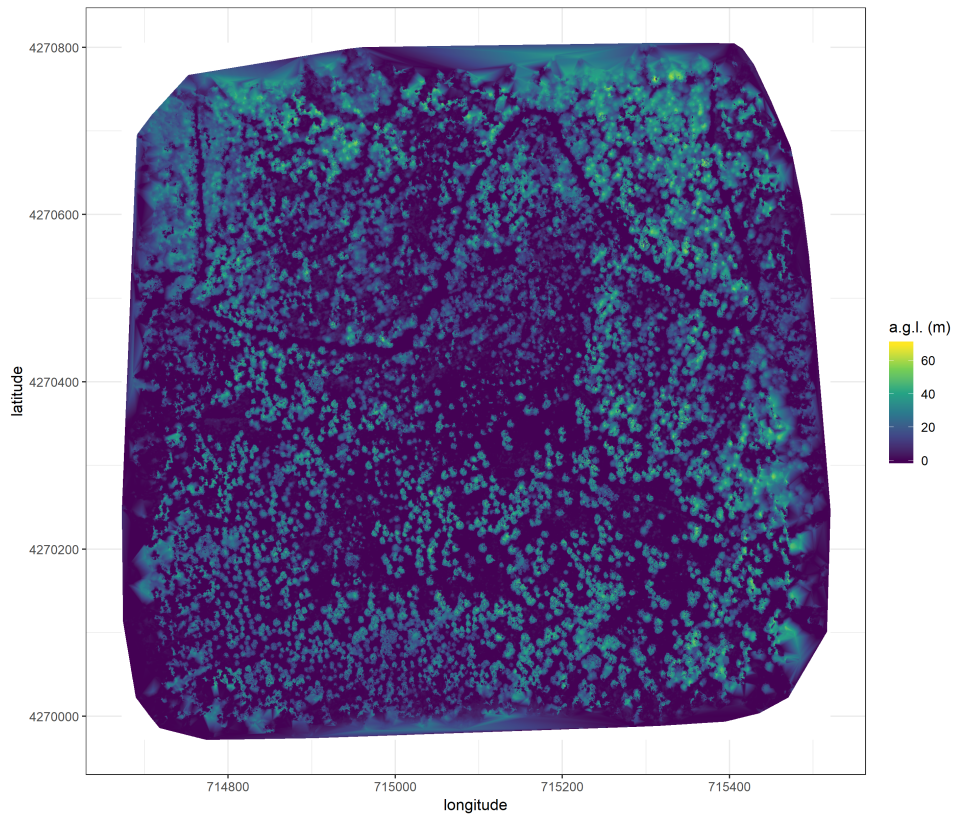


Figure 4: Example canopy height model (CHM) generated by subtracting the digital terrain model from the digital surface model. The CHM represents the height of all of the elevation above ground level.

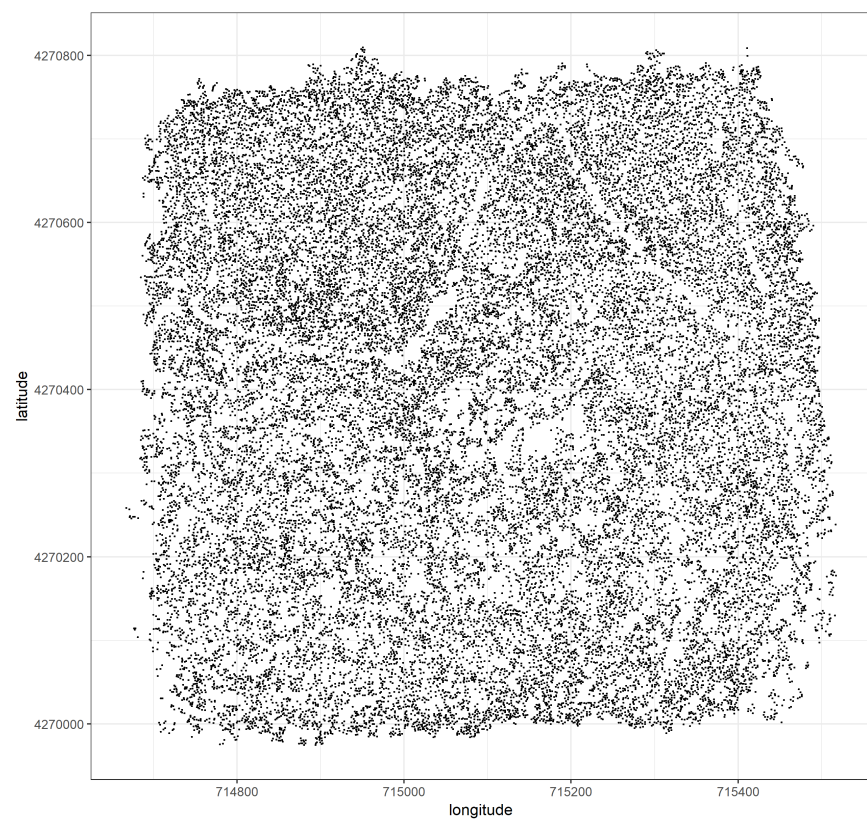


Figure 5: Tree top detection

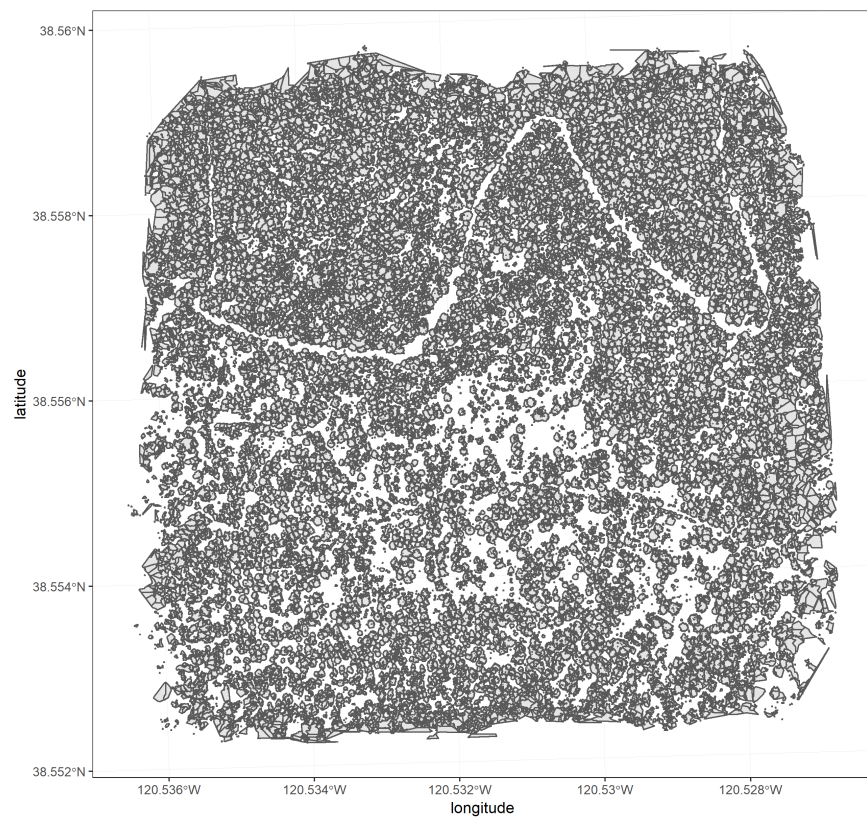


Figure 6: Crown segmentation

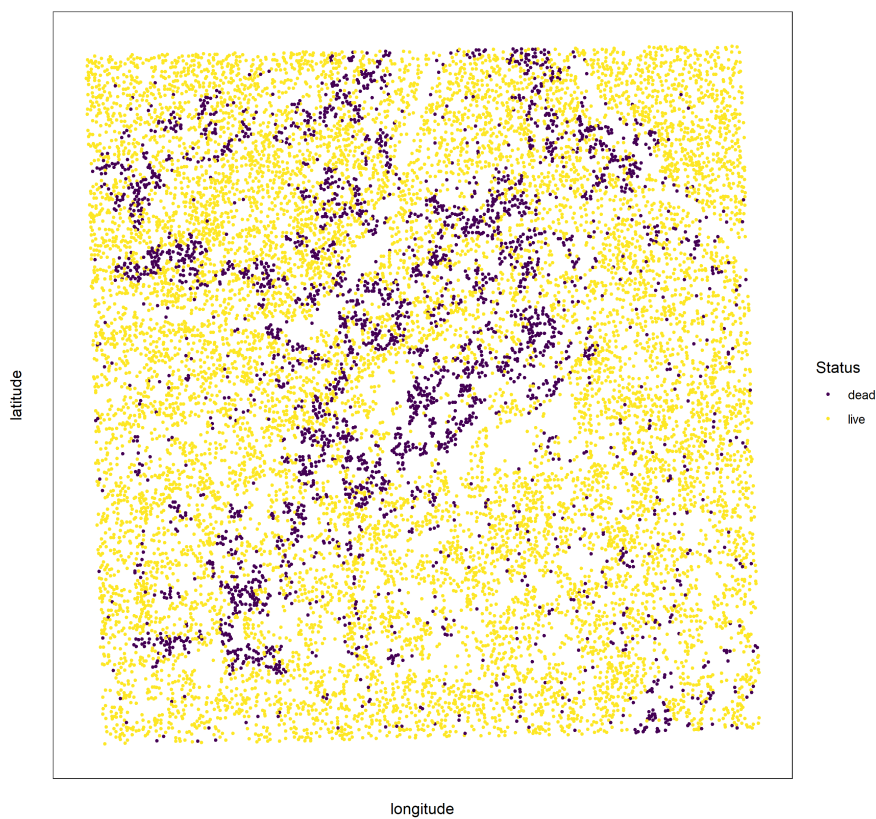


Figure 7: Live/dead classification

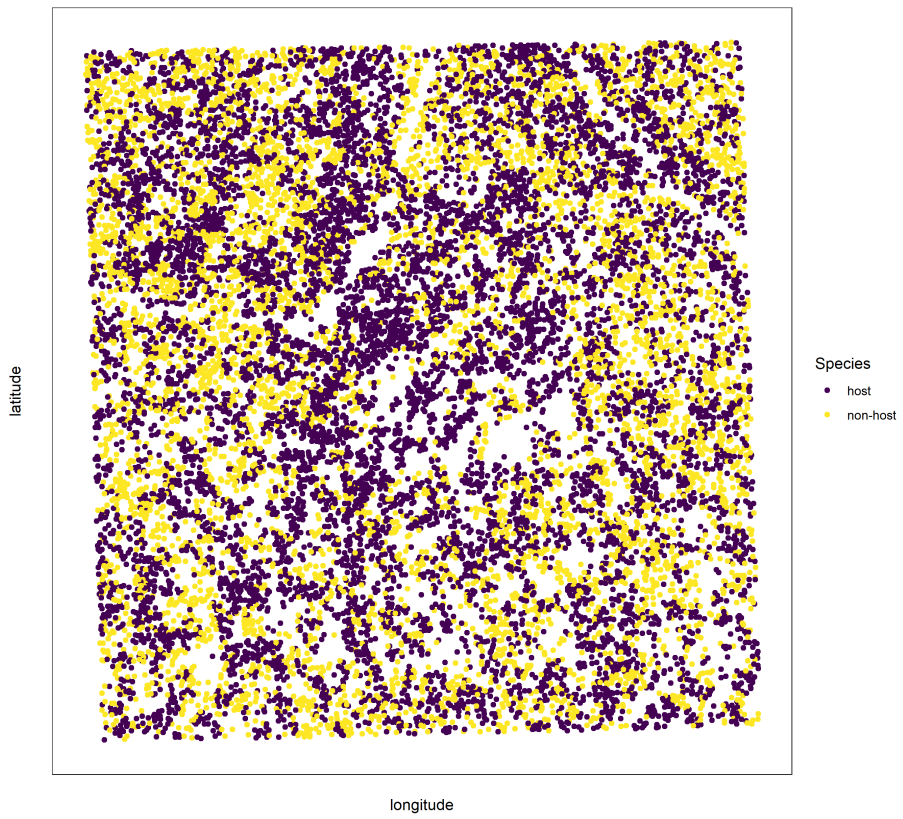


Figure 8: Host/non-host classification

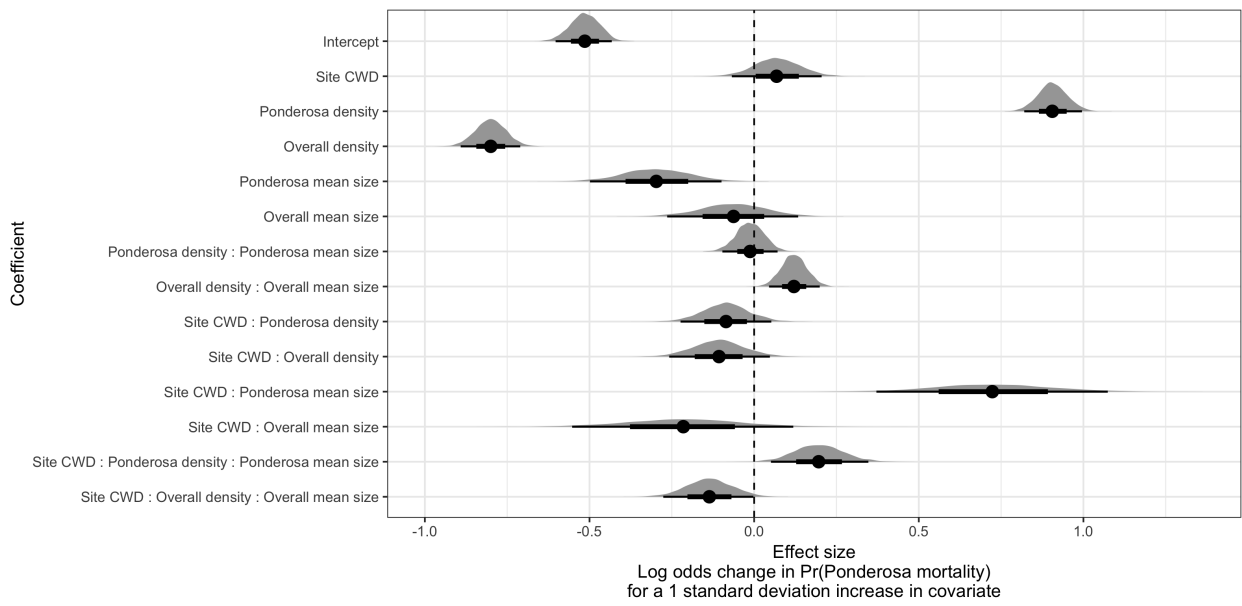


Figure 9: Halfeye plot showing posterior distributions of the effect sizes for the model

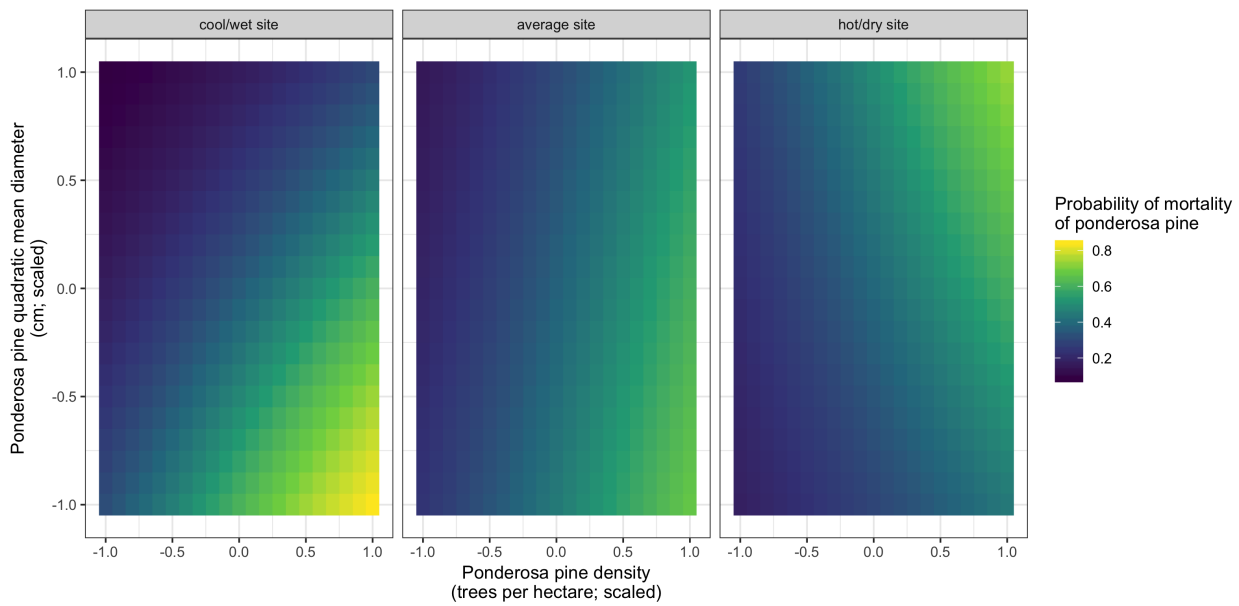


Figure 10: Raster version of model results showing the primary influence of Ponderosa pine structure on the probability of ponderosa pine mortality, and the interaction across climatic water deficit

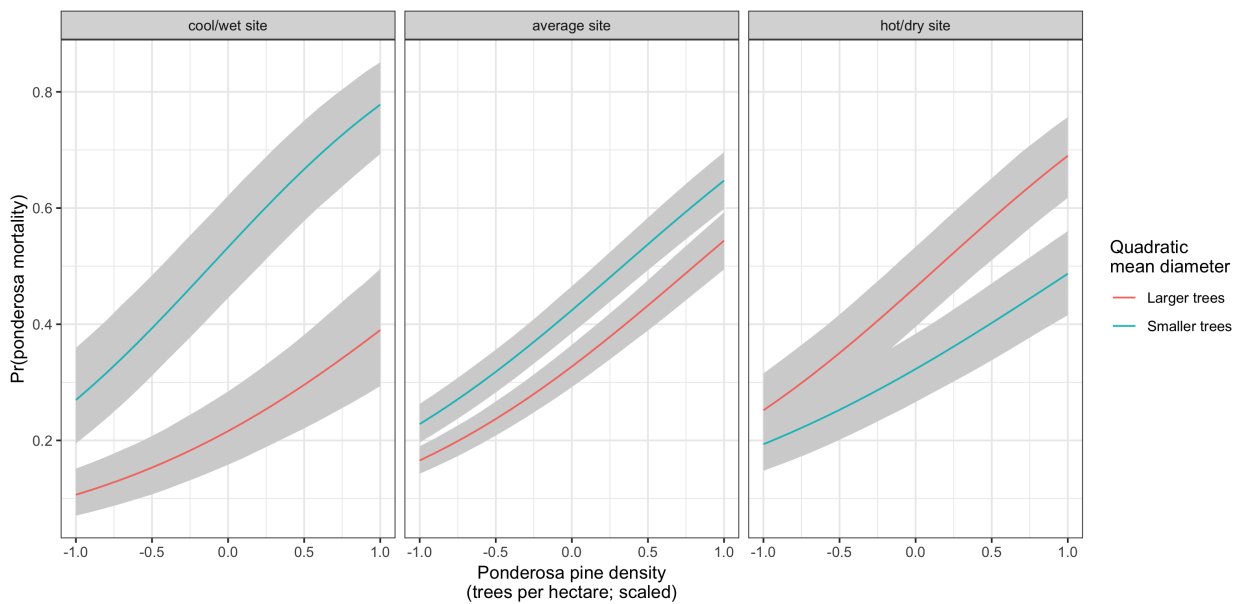


Figure 11: Line version with credible intervals showing primary influence of Ponderosa pine structure on the probability of ponderosa pine mortality, and the interaction across climatic water deficit

268 **Results**

269 **Tree detection**

270 We found that the experimental `lmfx` algorithm with parameter values of `dist2d = 1` and `ws = 2.5` (Roussel
271 et al. 2019) performed the best across 7 measures of forest structure as measured by Pearson's correlation
272 with ground data (Table 2).

273 Table 2: Correlation and differences between the best performing
tree detection algorithm (`lmfx` with `dist2d = 1` and `ws = 2.5`) and the
ground data. An asterisk next to the correlation or RMSE indicates
that this value was within 5% of the value of the best-performing
algorithm/parameter set.

Forest structure metric	Correlation with ground	RMSE	Mean error	Median error
height (m); 25th percentile	0.16	8.46	-2.30	-1.16
height (m); mean	0.29	7.81*	-3.43	-2.29
height (m); 75th percentile	0.35	10.33*	-4.85	-3.98
dist to 1st nearest neighbor (m)	0.55*	1.16*	0.13	0.26
dist to 2nd nearest neighbor (m)	0.61*	1.70*	0.08	0.12
dist to 3rd nearest neighbor (m)	0.50	2.29	0.17	0.19
total tree count	0.67*	8.68*	0.37	2.00
count of trees > 15m	0.43	7.38	1.18	0.00
count of trees < 15m	0.58	8.42	-0.66	2.00

274 **Effect of local structure on western pine beetle severity**

275 We found no main effect of climatic water deficit on the probability of ponderosa pine mortality within each
20m x 20m cell.

276 We found a strong effect of ponderosa pine local density, accounting for quadratic mean diameter, with
277 greater ponderosa pine density increasing the probability of ponderosa pine mortality. Conversely, we found
278 a generally negative effect of quadratic mean diameter of ponderosa pine on the probability of ponderosa
279 mortality, suggesting that the western pine beetle attacked smaller trees, on average. There was a strong
280 positive interaction between the climatic water deficit and ponderosa pine quadratic mean diameter, such

281 that larger trees were more likely to increase the probability of ponderosa mortality in hotter, drier sites.
282 We found negative main effects of overall tree density and overall quadratic mean diameter. There was a
283 positive interaction between these variables, such that denser stands with larger trees did lead to greater
284 ponderosa pine mortality.

285 **Spatial effects**

286 We were able to calculate the length scale of the spatial autocorrelation in the probability of ponderosa
287 pine mortality at each site, accounting for forest structure and environmental factors. By fitting a separate
288 approximate Gaussian process for each site on the interacting variables of the x- and y- position, we measured
289 the spatial covariance inherent in the data, accounting for other factors.

290 (Seidl et al. 2015) (Preisler et al. 2017)

291 **Discussion**

292 **Similarities and differences with Fettig et al. (2019)**

293 Fettig et al. (2019) found positive relationship between number of trees killed and: total number of trees,
294 total basal area, stand density index.

295 Fettig et al. (2019) found negative relationship between the proportion of trees killed and: total number of
296 trees, stand density index.

297 Hayes et al. (2009) and Fettig et al. (2019) found measures of host availability explained less variation in
298 mortality than measures of stand density.

299 Negrón et al. (2009) reported positive association of probability of ponderosa pine mortality and tree density
300 during a drought in Arizona.

301 Effect of competition may be masked because drought was so extreme Fettig et al. (2019); Floyd et al.
302 (2009), which is perhaps why we saw a counter-intuitive signal of increasing total basal area leading to lower
303 probability of ponderosa pine mortality.

304 **Broader context around field plots**

305 We surveyed 9 square kilometers of forest representing XXXXXX trees along a broad gradient. Site selection
306 and small plot size can influence inference. For instance, Fettig et al. (2019) reported statistically undetectable

307 differences in overall mortality in their plot network across 4 national forests. By expanding the hectarage
308 surveyed by a factor of 200, we detected dramatic differences in overall mortality.

309 This is about more than sample size. This is also about capturing the local disturbance phenomenon.

310 **310 Closer spacing between potential host trees facilitates dispersal**

311 If this drives mortality patterns, then we'd expect the count of ponderosa pine trees, accounting for other
312 variables, to have a strong positive effect.

313 **313 Host preference for large trees**

314 If this drives mortality patterns, then we'd expect the quadratic mean diameter of ponderosa pine trees,
315 accounting for other variables, to have a strong positive effect.

316 **316 Denser forests augment pheromone communication**

317 If this drives mortality patterns, then we'd expect the count of all trees, accounting for other variables, to
318 have a strong positive effect.

319 **319 Tree crowding leads to greater average water stress per tree**

320 If this drives mortality patterns, then we'd expect the quadratic mean dimater of all trees, accounting for
321 other factors, to have a strong positive effect.

322 **322 Interaction between host density and host size**

323 A positive coefficient would indicate a combined effect of WPB preference for large trees and nearby host
324 availability.

325 **325 Interaction between all tree density and all tree size**

326 A positive coefficient would indicate a combined effect of tree crowding and pheromone communication
327 enhancement.

328 **328 Interactions with climatic water deficit**

329 Are any of the above mechanisms exacerbated by water stress of the trees?

330 Spatial effect

331 The western pine beetle is known to exhibit strong aggregation and anti-aggregation behavior arising from
332 its pheromone communication, and thus it is likely that the measured spatial covariance in this study is
333 attributable to the magnitude of this effect at each site.

334 Some studies have suggested that “outbreak” conditions are distinguishable by clustered tree mortality, but
335 this is perhaps challenging to tease apart (Raffa et al. 2008). Our modeling framework allows for a joint
336 estimation of the effects of forest structure, environmental condition, and the spatial effect. This framework
337 would be enhanced with confidence in individual tree level data, and a lot of it, along with a strong gradient
338 of environmental conditions and forest structure.

339 We won’t interpret this measure of contagion, because the uncertainties in this particular study are too great
340 (tree detection, species classification, dead trees all assumed to be WPB hosts, didn’t account for topographic
341 effects which could also manifest as part of this spatial covariance process). But suggest that this could be a
342 meaningful and quantifiable

343 Important considerations

344 Cumulative effect of elevated insect activity, as mortality was spread out over 5 years and we surveyed at the
345 end. All the detected dead trees were considered ponderosa pine— we know this is wrong.’

346 Room for improvement

- 347 • Better geometry by using higher overlap, more spatially resolved images.
- 348 • Better image classification and scalability by using instrumentation having spectral overlap with more
349 widely deployed instrumentation (e.g., Landsat).
- 350 • Better tree detection using

351 Future directions

352 My goal is to tease apart the relative role of environmental drivers versus behavioral drivers of bark beetle-
353 induced tree mortality. I think teasing these apart will help with inference about the mechanism underlying
354 the effect of forest structure on disturbance severity. Crowded forests means trees are both water stressed
355 and are closer targets for new attacks [i.e., shorter dispersal needed to attack the next tree], and I think
356 comparing the “voronoi polygon area” effect with the “spatial covariance of mortality kernel” effect across
357 sites will tell us whether it’s the water stress or the smaller dispersal requirements driving mortality patterns.
358 A big voronoi polygon area effect and a short covariance kernel tells us that it’s a water stress effect— a

359 crowded tree gets attacked regardless of whether nearby trees were attacked. A small voronoi polygon area
360 effect and a long covariance kernel tells us that the mortality is patterned more based on there being spillover
361 from nearby attacked neighbors instead of how crowded any given tree is. I expect we might see different
362 relative magnitudes of voronoi polygon area and covariance kerenel effects depending on CWD.

363 **References**

- 364 Baldwin, B. G., A. H. Thornhill, W. A. Freyman, D. D. Ackerly, M. M. Kling, N. Morueta-Holme, and B. D.
365 Mishler. 2017. Species richness and endemism in the native flora of California. *American Journal of Botany*
366 104:487–501.
- 367 Brooks, S. P., and A. Gelman. 1998. General Methods for Monitoring Convergence of Iterative Simulations.
368 *Journal of Computational and Graphical Statistics* 7:434.
- 369 Bürkner, P.-C. 2017. **Brms** : An *R* Package for Bayesian Multilevel Models Using *Stan*. *Journal of Statistical*
370 *Software* 80.
- 371 Clevers, J., and A. Gitelson. 2013. Remote estimation of crop and grass chlorophyll and nitrogen content using
372 red-edge bands on Sentinel-2 and -3. *International Journal of Applied Earth Observation and Geoinformation*
373 23:344–351.
- 374 Coops, N. C., M. Johnson, M. A. Wulder, and J. C. White. 2006. Assessment of QuickBird high spatial
375 resolution imagery to detect red attack damage due to mountain pine beetle infestation. *Remote Sensing of*
376 *Environment* 103:67–80.
- 377 DJI. 2015a. Zenmuse X3 - Creativity Unleashed. <https://www.dji.com/zenmuse-x3/info>.
- 378 DJI. 2015b. DJI - The World Leader in Camera Drones/Quadcopters for Aerial Photography. <https://www.dji.com/matrice100/info>.
- 380 Easy, D. M. 2018. Map Pilot for DJI. <https://itunes.apple.com/us/app/map-pilot-for-dji/id1014765000?mt=8>.
- 381 Eysn, L., M. Hollaus, E. Lindberg, F. Berger, J.-M. Monnet, M. Dalponte, M. Kobal, M. Pellegrini, E.
382 Lingua, D. Mongus, and N. Pfeifer. 2015. A Benchmark of Lidar-Based Single Tree Detection Methods Using
383 Heterogeneous Forest Data from the Alpine Space. *Forests* 6:1721–1747.
- 384 Farr, T. G., P. A. Rosen, E. Caro, R. Crippen, R. Duren, S. Hensley, M. Kobrick, M. Paller, E. Rodriguez, L.
385 Roth, D. Seal, S. Shaffer, J. Shimada, J. Umland, M. Werner, M. Oskin, D. Burbank, and D. Alsdorf. 2007.

- 386 The Shuttle Radar Topography Mission. *Reviews of Geophysics* 45.
- 387 Fettig, C. J. 2012. Chapter 2: Forest health and bark beetles. *in* Managing Sierra Nevada Forests. PSW-
- 388 GTR-237. USDA Forest Service.
- 389 Fettig, C. J., L. A. Mortenson, B. M. Bulaon, and P. B. Fulk. 2019. Tree mortality following drought in the
- 390 central and southern Sierra Nevada, California, U.S. *Forest Ecology and Management* 432:164–178.
- 391 Flint, L. E., A. L. Flint, J. H. Thorne, and R. Boynton. 2013. Fine-scale hydrologic modeling for regional land-
- 392 scape applications: The California Basin Characterization Model development and performance. *Ecological*
- 393 *Processes* 2:25.
- 394 Floyd, M. L., M. Clifford, N. S. Cobb, D. Hanna, R. Delph, P. Ford, and D. Turner. 2009. Relationship of
- 395 stand characteristics to drought-induced mortality in three Southwestern piñonJuniper woodlands. *Ecological*
- 396 *Applications* 19:1223–1230.
- 397 Gabry, J., D. Simpson, A. Vehtari, M. Betancourt, and A. Gelman. 2019. Visualization in Bayesian workflow.
- 398 *Journal of the Royal Statistical Society: Series A (Statistics in Society)* 182:389–402.
- 399 Gitelson, A., and M. N. Merzlyak. 1994. Spectral Reflectance Changes Associated with Autumn Senescence
- 400 of *Aesculus hippocastanum* L. and *Acer platanoides* L. Leaves. Spectral Features and Relation to Chlorophyll
- 401 Estimation. *Journal of Plant Physiology* 143:286–292.
- 402 Hayes, C. J., C. J. Fettig, and L. D. Merrill. 2009. Evaluation of Multiple Funnel Traps and Stand
- 403 Characteristics for Estimating Western Pine Beetle-Caused Tree Mortality. *Journal of Economic Entomology*
- 404 102:2170–2182.
- 405 Hijmans, R. J., J. van Etten, M. Sumner, J. Cheng, A. Bevan, R. Bivand, L. Busetto, M. Canty, D. Forrest,
- 406 A. Ghosh, D. Golicher, J. Gray, J. A. Greenberg, P. Hiemstra, I. for M. A. Geosciences, C. Karney, M.
- 407 Mattiuzzi, S. Mosher, J. Nowosad, E. Pebesma, O. P. Lamigueiro, E. B. Racine, B. Rowlingson, A. Shortridge,
- 408 B. Venables, and R. Wueest. 2019. *Raster: Geographic Data Analysis and Modeling*.
- 409 Hunziker, P. 2017. *Velox: Fast Raster Manipulation and Extraction*.
- 410 Jakubowski, M. K., W. Li, Q. Guo, and M. Kelly. 2013. Delineating Individual Trees from Lidar Data: A
- 411 Comparison of Vector- and Raster-based Segmentation Approaches. *Remote Sensing* 5:4163–4186.
- 412 Kane, V. R., M. P. North, J. A. Lutz, D. J. Churchill, S. L. Roberts, D. F. Smith, R. J. McGaughey, J. T.
- 413 Kane, and M. L. Brooks. 2014. Assessing fire effects on forest spatial structure using a fusion of Landsat and

- ⁴¹⁴ airborne LiDAR data in Yosemite National Park. *Remote Sensing of Environment* 151:89–101.
- ⁴¹⁵ Kuhn, M. 2008. Building Predictive Models in R Using the caret Package. *Journal of Statistical Software* 28:1–26.
- ⁴¹⁷ Larson, A. J., and D. Churchill. 2012. Tree spatial patterns in fire-frequent forests of western North America, including mechanisms of pattern formation and implications for designing fuel reduction and restoration treatments. *Forest Ecology and Management* 267:74–92.
- ⁴²⁰ Li, W., Q. Guo, M. K. Jakubowski, and M. Kelly. 2012. A New Method for Segmenting Individual Trees from the Lidar Point Cloud. *Photogrammetric Engineering & Remote Sensing* 78:75–84.
- ⁴²² Meyer, F., and S. Beucher. 1990. Morphological segmentation. *Journal of Visual Communication and Image Representation* 1:21–46.
- ⁴²⁴ Micasense. 2015. MicaSense. <https://support.micasense.com/hc/en-us/articles/215261448-RedEdge-User-Manual-PDF-Download>
- ⁴²⁵ Millar, C. I., and N. L. Stephenson. 2015. Temperate forest health in an era of emerging megadisturbance. *Science* 349:823–826.
- ⁴²⁷ Morris, J. L., S. Cottrell, C. J. Fettig, W. D. Hansen, R. L. Sherriff, V. A. Carter, J. L. Clear, J. Clement, R. J. DeRose, J. A. Hicke, P. E. Higuera, K. M. Mattor, A. W. R. Seddon, H. T. Seppä, J. D. Stednick, and S. J. Seybold. 2017. Managing bark beetle impacts on ecosystems and society: Priority questions to motivate future research. *Journal of Applied Ecology* 54:750–760.
- ⁴³¹ Negrón, J. F., J. D. McMillin, J. A. Anhold, and D. Coulson. 2009. Bark beetle-caused mortality in a drought-affected ponderosa pine landscape in Arizona, USA. *Forest Ecology and Management* 257:1353–1362.
- ⁴³³ North, M. P., S. L. Stephens, B. M. Collins, J. K. Agee, G. Aplet, J. F. Franklin, and P. Z. Fule. 2015. Reform forest fire management. *Science* 349:1280–1281.
- ⁴³⁵ Pau, G., F. Fuchs, O. Sklyar, M. Boutros, and W. Huber. 2010. EBImagean R package for image processing with applications to cellular phenotypes. *Bioinformatics* 26:979–981.
- ⁴³⁷ Pebesma, E., R. Bivand, E. Racine, M. Sumner, I. Cook, T. Keitt, R. Lovelace, H. Wickham, J. Ooms, K. Müller, and T. L. Pedersen. 2019. Sf: Simple Features for R.
- ⁴³⁹ Plowright, A. 2018. ForestTools: Analyzing Remotely Sensed Forest Data.
- ⁴⁴⁰ Popescu, S. C., and R. H. Wynne. 2004. Seeing the Trees in the Forest: Using Lidar and Multispectral Data Fusion with Local Filtering and Variable Window Size for Estimating Tree Height. *PHOTOGRAMMETRIC*

- 442 ENGINEERING:16.
- 443 Preisler, H. K., N. E. Grulke, Z. Heath, and S. L. Smith. 2017. Analysis and out-year forecast of beetle,
444 borer, and drought-induced tree mortality in California. *Forest Ecology and Management*. 399: 166-178
445 399:166–178.
- 446 R Core Team. 2018. R: A Language and Environment for Statistical Computing. R Foundation for Statistical
447 Computing, Vienna, Austria.
- 448 Raffa, K. F., B. H. Aukema, B. J. Bentz, A. L. Carroll, J. A. Hicke, M. G. Turner, and W. H. Romme. 2008.
449 Cross-scale Drivers of Natural Disturbances Prone to Anthropogenic Amplification: The Dynamics of Bark
450 Beetle Eruptions. *BioScience* 58:501–517.
- 451 Rouse, W., R. H. Haas, W. Deering, and J. A. Schell. 1973. MONITORING THE VERNAL ADVANCEMENT
452 AND RETROGRADATION (GREEN WAVE EFFECT) OF NATURAL VEGETATION. Type II Report,
453 Goddard Space Flight Center, Greenbelt, MD, USA.
- 454 Roussel, J.-R. 2019. lidRplugins: Extra functions and algorithms for lidR package.
- 455 Roussel, J.-R., D. A. (. the documentation), F. D. B. (. bugs and improved catalog features), and A. S. M. (.
456 lassnags). 2019. lidR: Airborne LiDAR Data Manipulation and Visualization for Forestry Applications.
- 457 Seidl, R., J. Müller, T. Hothorn, C. Bässler, M. Heurich, and M. Kautz. 2015. Small beetle, large-scale
458 drivers: How regional and landscape factors affect outbreaks of the European spruce bark beetle. *The Journal
459 of applied ecology* 53:530–540.
- 460 Shin, P., T. Sankey, M. Moore, and A. Thode. 2018. Evaluating Unmanned Aerial Vehicle Images for
461 Estimating Forest Canopy Fuels in a Ponderosa Pine Stand. *Remote Sensing* 10:1266.
- 462 Stephenson, N. 1998. Actual evapotranspiration and deficit: Biologically meaningful correlates of vegetation
463 distribution across spatial scales. *Journal of Biogeography* 25:855–870.
- 464 USDAFS. 2019, February 11. Press Release: Survey finds 18 million trees died in California in 2018.
465 https://www.fs.usda.gov/Internet/FSE_DOCUMENTS/FSEPRD609321.pdf.
- 466 Vega, C., A. Hamrouni, S. El Mokhtari, J. Morel, J. Bock, J. P. Renaud, M. Bouvier, and S. Durrieu. 2014.
467 PTrees: A point-based approach to forest tree extraction from lidar data. *International Journal of Applied
468 Earth Observation and Geoinformation* 33:98–108.
- 469 Young, D. J. N., J. T. Stevens, J. M. Earles, J. Moore, A. Ellis, A. L. Jirka, and A. M. Latimer. 2017.
470 Long-term climate and competition explain forest mortality patterns under extreme drought. *Ecology Letters*

⁴⁷¹ 20:78–86.

⁴⁷² Zhang, W., J. Qi, P. Wan, H. Wang, D. Xie, X. Wang, and G. Yan. 2016. An Easy-to-Use Airborne LiDAR
⁴⁷³ Data Filtering Method Based on Cloth Simulation. *Remote Sensing* 8:501.